DEVELOPMENT OF A NEW MEDIUM SIZE HELICOPTER WIND TUNNEL MODEL

Oliver Schneider, DLR, Institute of Flight Systems, Braunschweig, Germany
Henning Mainz, DLR, Institute of Flight Systems, Braunschweig, Germany
Erik Brehl, DLR, Institute of Flight Systems, Braunschweig, Germany
Sascha Henseleit-Wieser, DLR, Institute of Flight Systems, Braunschweig, Germany
Berend G. van der Wall, DLR, Institute of Flight Systems, Braunschweig, Germany

Abstract

In the framework of the DLR guiding concept "The Rescue Helicopter 2030" a new medium size wind tunnel model was developed at DLR. The development of the new wind tunnel model was finished in 2024.In this paper background information of first ideas and final model design, of model scaling, and manufacturing of parts are given. The pre-testing of individual components and the complete model is described. Furthermore, insights for model instrumentation, load balance design, as well as for different data acquisition systems are included and preliminary results from first experiments and from two wind tunnel tests are presented.

1. NOTATION

Symbols

F_x	Rotor horizontal force, N
F_z	Rotor vertical force, N
P	Rotor power, kW
R	Rotor radius, m
C_P	Rotor power coefficient, -
C_T	Rotor thrust coefficient, -
Θ_{75}	Blade pitch angle at $75\%\ R$, deg
α	Fuselage angle of attack, deg
β	Fuselage yaw angle, deg
σ	Rotor solidity, -
Ω	Rotor speed, rad/s

Acronyms:

ATTILA	Advanced Testbed for TILtrotor Aeroelastics
B&R	Bernecker + Rainer Industrie-Elektronik GmbH
DAQ	Data Acquisition System
DNW	German Dutch Wind Tunnels
DLR-FT	DLR Institute of Flight Systems
FM	Figure of merit
HMI	Human Machine Interface
LLF	Large Low Speed Facility
NEXTTRIP	NEXT generation civil Tilt Rotor Interactional aerodynamic tail oPtimisation
NWB	Low Speed Wind-Tunnel Braunschweig
PCB	Printed circuit boards
PGA	Programmable gain amplifiers
REF	Reference configuration
RTG	Rotor Test-stand Göttingen
RTM	Resin Transfer Moulding
SPR	Stereo pattern recognition
SZ-1	Scenario 1
TEDAS	Throughput Enhanced Data Acquisition System

2. INTRODUCTION

Testing of helicopter models in wind tunnels is a challenging task, but very helpful for improvements of design tools by extension of the theoretical models. It is also beneficial for a shorter development cycle for new helicopter configurations and the overall risk

reduction during that process. The DLR Institute of Flight Systems is operating different helicopter wind tunnel models since 1978. For single blade laboratory testing a whirl tower is available on site for rotors up to $R = 2.5\,m$ radius. Design target of these models with a rotor radius of up to $R = 2.1\,m$ was the operation in the DNW-LLF in the Netherlands. They were used to get more knowledge in various topics like rotor wakes, acoustics, vibrations (Ref 1, Ref 2), and power requirements of isolated Mach-scaled main and tail rotors or complete helicopter configurations as well as fuselage aerodynamics, flow characteristics or configuration changes (Ref 3). New control technologies like higher harmonic control or individual blade control were investigated in the past as well (Ref 4). The team of the rotor test rig facility is also participating in wind tunnel tests with international partners using external models. In the EU-project NEXTTRIP (Ref 5) the aerodynamics of a full tilt-rotor model was investigated in 2014, the whirl flutter stability of a tilt-rotor half model was the objective of the ATTILA wind tunnel test campaign, which was conducted in two different tests in 2023 (see Ref 6).

To get further capabilities in wind tunnel testing now a new model was designed and manufactured for use in smaller wind tunnels like DNW-NWB with a cross section of $3.25\,m\ x\ 2.8\,m$. The results obtained by the new test rig are partly also comparable with experiments carried out at the RTG (Ref 7). The development of the model took place in basic funded DLR projects and was finished in June 2024.

In the framework of the DLR guiding concept “The Rescue Helicopter 2030” two different fuselages were designed for comparison of aerodynamic performance and a first wind tunnel test was conducted in 2020 (Figure 1). In the further development a second wind tunnel test was conducted in 2024 including rotor system and additional wings. The guiding concept aims for future helicopters which should be able to reach their destination quickly, safely, quietly and flexibly, over longer distances than today, and regardless of weather conditions. The basic dimensions of the rig of 1.0 $m\ x$ 0.3 $m\ x$ 0.4 m make it possible to mount scaled fuselages of conventional or modern design.

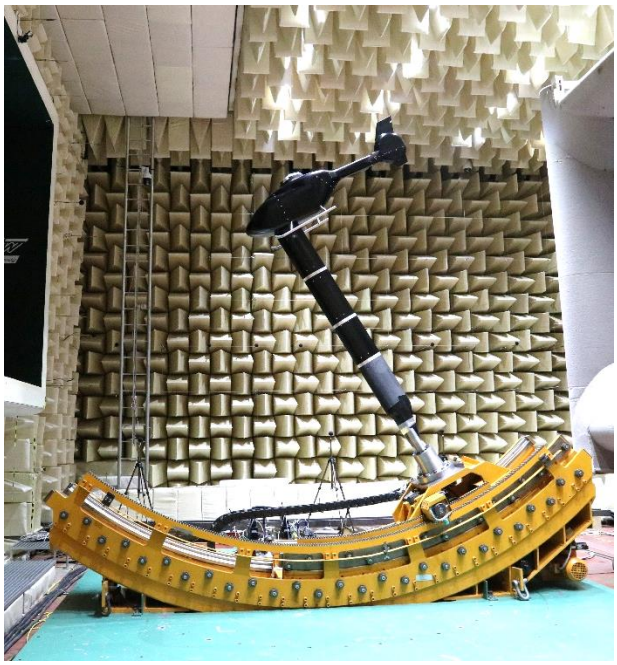

Figure 1: Wind tunnel test at DNW-NWB in 2020 with the REF-configuration

3. MODEL DESIGN AND CONSTRUCTION

Developing a completely new wind tunnel model is a very challenging mission. The development is split into different phases starting with model scaling and definitions, followed by the design and construction of the different parts.

3.1. Specifications and scaling

At the very beginning of the design process the specifications and model scaling were agreed between all institutes involved in the project. The scaling is based on the test section size of the DNW-NWB wind tunnel which is $3.25\,m\ x\ 2.8\,m$. To prevent too much blockage of the flow and influences from the wind tunnel walls a rotor diameter of $1.6\,m$ was chosen, which corresponds to half the test section width. The refence helicopter configuration REF is based on an EC-135 of Airbus Helicopters with a rotor diameter of $10.2\,m$. Thus, the initial model scaling factor was 6.375. To compare aerodynamic and areo-acoustic phenomena Mach scaling is used for the rotor system. In the course of the design the rotor radius had to be increased slightly by $12\,mm$ because of space constrains in the rotor hub. The final model specifications are shown in *Table 1*.

Table 1: Main model specifications

Parameter	symbol / unit	value
Rotor diameter	$R\ /\ m$	1.624
Tip speed	$v_{Tip}\ /\ m/s$	211
Angular velocity	$\Omega\ /\ rad/s$	260
Rotor speed	$n\ /\ rpm$	2481
Tip Mach number	$Ma_{Tip}\ /\ -$	0.615
Nominal thrust	$T\ /\ N$	724
Blade mean chord	$c\ /\ mm$	57
Desired rotor power	$P\ /\ kW$	50
Rotor system		hingeless
Pre-cone angle	$\beta_{pre}\ /\ deg$	2.0
Sense of rotation		counterclock-wise
Model attachment		belly sting

3.2. Balance setup

To separate the measurement of different load sources, it was necessary to use different balances. The balance setup is shown in Figure 2. The rotor balance (RUAG 192-6D) is directly attached to the belly sting using a flange. The rotor balance carries the complete base structure including hydraulic motor and drive system as well as the rotor system.

For measuring the fuselage loads an integrated cylindrical balance of type Task 1.25" is integrated behind the rotor shaft. The connection of the fuselage balance to the sting attachment point is done via two structure side plates outside the basic structure to guarantee independent measurements of rotor and fuselage loads.

Depending on the two configurations REF (Figure 3) or SZ-1 (Figure 4) either two 3-component stabilizer balances are connected to the rear fuselage, as shown in Figure 2, or two 5-component wing balances can be mounted to the side of the side plates (see Figure 4) and measured independently from rotor and fuselage balance.

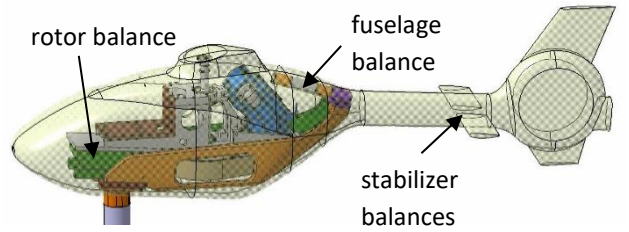

Figure 2: Balance setup

3.3. Fuselages (+ Wings)

Two different fuselages were of interest. The reference fuselage (REF), representing a state-of-the-art helicopter with Fenestron configuration similar to an Airbus Helicopters EC135, was equipped with a horizontal stabilizer and skids, as shown in Figure 3. The second fuselage is called SZ-1 (scenario 1) and is based on a newly optimized design for a conventional rescue helicopter, with a design as can be seen in Figure 4. A fuselage shape was designed for improved aerodynamics and less total drag to increase the flight envelope and reduce the necessary rotor power. Furthermore, the rotor is relieved of thrust in high speed conditions by additional wings. The wings are mounted on a rod which is connected to the side plate of the basic structure without mechanical contact to the fuselage. Each wing can manually be rotated around its c/4 axis to adjust the inclination angle relative to the fuselage. During operation the wing angle is fixed by two clamps.

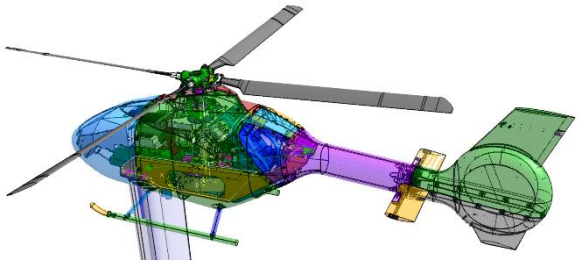

Figure 3: REF configuration with skids

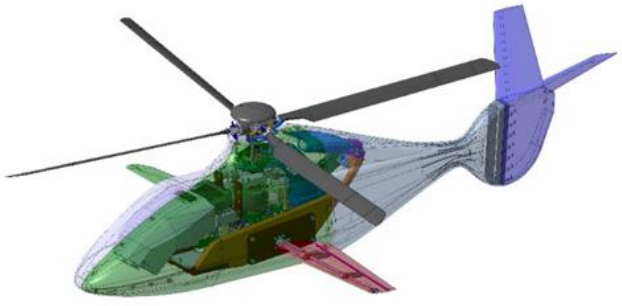

Figure 4: SZ-1 configuration without skids

3.4. Rotor hub system

For the new wind tunnel model, it was decided to use a 4-bladed hingeless rotor hub configuration with conventional swash-plate control. The rotor hub system is shown in Figure 5.

For blade pitch angle adjustment needle bearings are in use, also carrying blade bending loads in flap and

lead-lag direction. Special slat packs are installed to carry the centrifugal loads of the rotor blades and allow pitch angle movements. On top of the rotor head an ellipsoid shaped housing is placed for installation of the rotating electronic components as well as the rotational DAQ system.

In the design phase a pre-cone angle of $2.0\,deg$ was defined to get minimal steady flap bending moments for the scaled thrust of $724\,N$ at nominal rotation speed.

For measurements with isolated fuselage, 4 blade stubs can be mounted instead of the rotor blades, such that only the blade root is present up to the beginning of the aerodynamic blade part, as can be seen in Figure 11 bottom. This is also useful for connection of the electronic cables between blades and rotor hub.

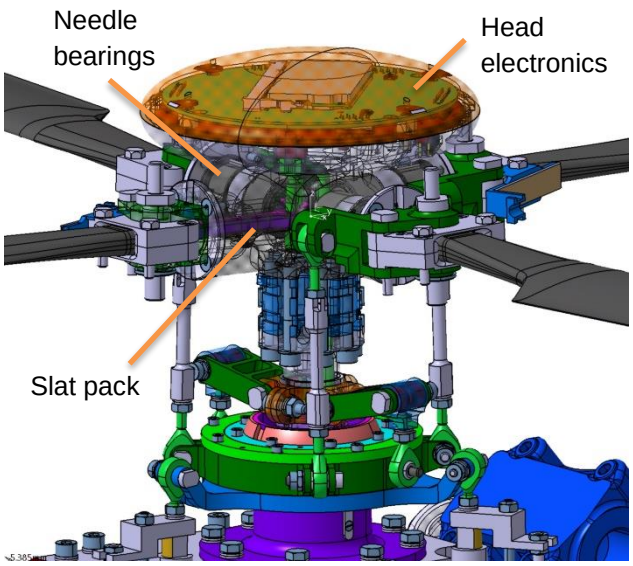

Figure 5: Rotor hub system

3.5. Drive system and model control

The main drive of the rotor system is designed to deliver up to $50\,kW$ of rotor power using a hydraulic motor (Bosch-Rexroth A2FM16) and a tooth belt drive with a gear ratio of 28:60. The hydraulic pressure and flow is provided by a power unit outside of the test hall, available to supply $160\,kW$ of electric power. A valve block is placed close to the model and connected to the power unit by means of tubes and houses. The rotor speed is adjusted using an automation system from B&R. The rpm control is done in closed loop configuration by software-based PID controllers based on main pump pressure, differential pressure between motor in- and output, and nominal and actual rotor speed. For the new model the B&R Power Panel PP580 is used, which takes over the computer power and the human-computer interface as the central controller in the rotor test rig. In addition to a touch screen, the Power Panel covers interfaces such as Ethernet, USB and RS232.

To control all components of the model a piloting rack is used, as shown in Figure 6. This rack includes the B&R panel in combination with the rpm control knob (bottom right), a special designed monitoring software to observe the most important sensors (bottom left), a screen with online data of selected time histories (top left) and a video screen showing the image of a radio-controlled network camera.

For control of the conventional swash-plate an electrical linear actuator system is used. Therefore, three stepper motors (MICROSTEP GmbH, azimuthally spaced 120°) are installed and driven by the HMI system, which is part of the piloting rack (see Figure 6 bottom left). On the one hand the microcontroller-based HMI system consists of a three rotating knob configuration for adjusting collective as well as sine and cosine pitch angle components. On the other hand, a small display is showing the current swash-plate settings and other helpful information about the actuators. An additional loudspeaker which transfers the sound of the test section is a very helpful tool for piloting to observe model conditions and recognize faults.

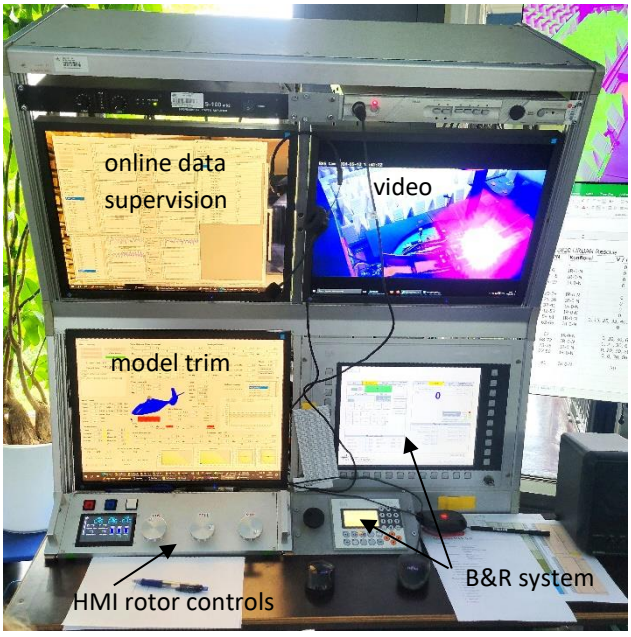

Figure 6: Piloting rack

4. MODEL MANUFACTURING

The main components like sting, basic structure, side plates, flanges, gears, swash-plate, rotor shaft and rotor head are manufactured at DLR using metallic materials (steel, aluminum). Components for covering electronics are partly made of 3D-printed material. Rotor blades are made of carbon fiber materials, as described in section 4.2.

4.1. Slat packs

The model is equipped with a hingeless rotor system. Special emphasis was given to the elements carrying the centrifugal loads of the rotor blades. Therefore, a pack of 29 slats (see Figure 7) per blade attachment is connected to the rotor head on one side and to the blade clamping part on the other side. One slat has a thickness of $0.2\,mm$. The shape of the single slats was optimized for uniform stress distribution. Furthermore, the outer three are different to the inner slats. In a bench test one slat pack was tested for long time using the expected load conditions for the different flight cases (cruise, high rpm, slowed rotor). The slat pack was loaded with different pull forces, simulating the centrifugal load during rotation. Furthermore, the cyclic pitch changes were simulated depending on the flight case. Test duration was 71 hours. In total 9.5 million load cycles were conducted and the slat pack proved the long-time stability.

Figure 7: Pack of slats

4.2. Rotor blades

Manufacturing of the rotor blades was done in-house. The blade skins were produced using the RTM method, a low-pressure closed moulding process, which leads to an accurate and good surface finish. Using two metal moulds the skins were produced first by infusion technology using carbon fibers. During this process markers were inserted to the outer side of the skin for measuring blade deformation by means of SPR (Ref 8, see Figure 10). The result of the first step can be seen in Figure 8. Seconds step is sensor installation to the inner side of the skins like strain gauges for torsion moment as well as the dynamic pressure sensors (Figure 9). For this set of rotor blades also tip LEDs were inserted to ease the blade tracking procedure.

Figure 8: Upper and lower blade skin

Main step is the blade assembly. Here, the blade spar is included to each side of the inner blade skins using fiber rovings which are saturated with resin in a special device and cut to length before inserting.

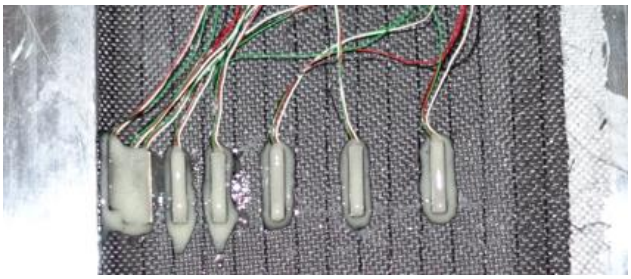

Figure 9: Pressure sensors in the upper skin

Finally, by a thermal treatment the inner structure of the blades is stabilized. After blade assembly (see Figure 10) further strain gauges are instrumented from outside for measuring flap and lead-lag bending moments. More detailed information on rotor blade manufacturing can be found in Ref 9.

Figure 10: Rotor bade after assembly

4.3. Fuselages

Parts of the reference fuselage like nose and vertical tail were printed with ULTEM 9085 thermoplastic material, the tail-boom section and side parts with FDM nylon 12CF reinforced thermoplastic. The wall thickness is 3 mm and the connection to the fuselage

balance is realized using an aluminum adapter, as can be seen in Figure 11 top.

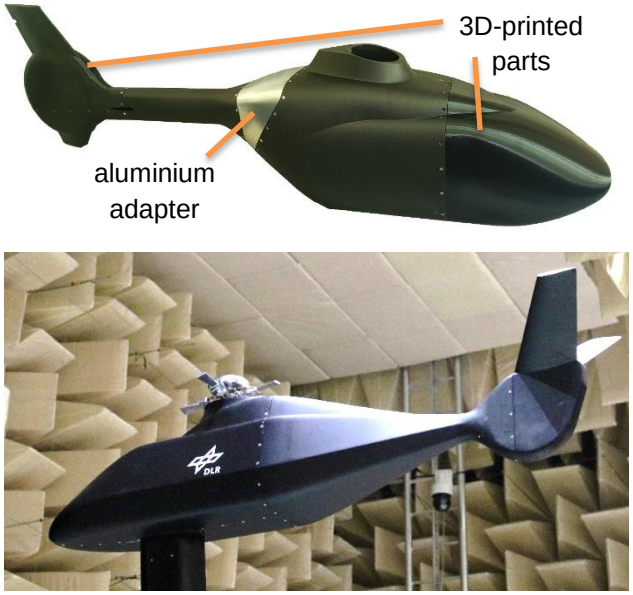

Figure 11: 3D-printed REF fuselage (top), SZ-1 fuselage (bottom)

The surface finishing is done by priming, grinding and finishing with a matt black top coat. The optimized SZ-1 fuselage is printed by MULTEC on a M800 FDM printer using PLA-HT filament (Figure 11 bottom). The additional wings and horizontal stabilizer airfoils are 3D-printed as well. To cover the wind tunnel sting streamlined airfoil shaped parts were manufactured, also using 3D-printing.

5. MODEL INSTRUMENTATION AND DAQ

5.1. Instrumentation

To guarantee safe model operation a lot of sensors are installed inside the model. They are necessary for observation of the model condition and to control and trim it properly. The instrumentation is divided in sensors in the non-rotating frame and sensors in the rotating frame.

Basic model loads are monitored by different load balances, like a 6-component rotor balance, a 6-component fuselage balance, two 5-component stabilizer balances and two 5-component wing balances. To avoid possible temperature effects the rotor balance is equipped with a heating system by means of heat foils on both sides. By using the B&R automation system a feedback controller ensures that the balance temperature remains at a nominal value all the time.

To measure the horizontal stabilizer loads of the reference fuselage new load balances were developed, based on strain gauges. Different designs were investigated to fit to the requirements and finally a Y-shaped configuration was chosen, as can be seen in Figure 12. Using this design 3 load components can be acquired: normal force, drag force, and pitching moment. The optimal position of strain gauges was determined by FEM analysis.

For the optimized SZ-1 fuselage the mounting of additional wings is possible. To get load information of these wings new balances were developed. By means of 5 strain gauge full bridges a 5-component balance is realized for each side to measure the pitching moment, lift and drag force as well as the positions were lift and drag force act on the wing. The strain gauge instrumentation is shown in Figure 13.

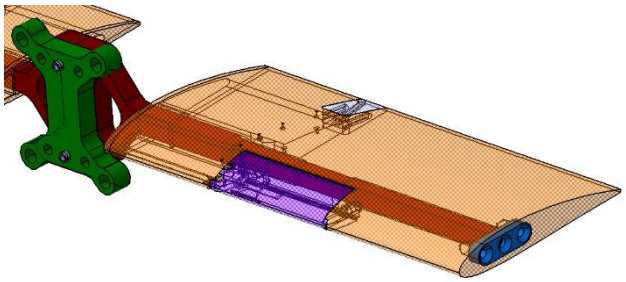

Figure 12: Horizontal stabilizer design

Figure 13: Wing balance strain gauge instrumentation

Both fuselages were equipped with surface sensors to measure static and dynamic pressures. The distribution of sensor locations for the reference configuration is shown in Figure 14. In total, 140 static and 20 dynamic pressure sensors were instrumented for the REF fuselage.

The SZ-1 fuselage was equipped with 46 static and 13 dynamic pressure sensors. Measuring static surface pressures is done by a Scanivalve system provided by DNW-NWB. In *Table 2* a summary of all model sensors is given.

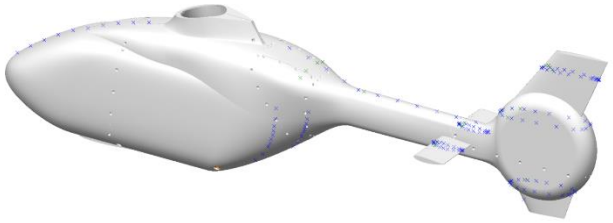

Figure 14: Pressure sensor locations REF-fuselage

Table 2: Model instrumentation

Sensor	Number	Type
non-rotating system		
Rotor balance	1	RUAG, 6 comp.
Fuselage balance	1	task, 6 comp.
Stabilizer balance (REF only)	2	3 components
Wing balances (SZ-1 only)	2	5 components
Accelerometer	3	3 axis (5g)
dynamic pressures fuselage	REF: 20 SZ-1: 13	Kulite
static pressures fuselage	REF: 140 SZ-1: 46	Scanivalve
actuator forces	3	strain gauges
temperatures	9	PT 100
angle encoder	1	Heidenhain
rotating system		
pitch link force	4	strain gauges
shaft bending	2	strain gauges
shaft torsion	1	strain gauges
pitch angle	4	potentiometer
blade bending moments	4 flap, 4 lag	strain gauges
blade torsion moments	4	strain gauges
dynamic blade pressures	14+8	Kulite / AS

5.2. Data acquisition non-rotating sensors

All data from sensors in the non-rotating frame are acquired by the in-house developed TEDAS III system (Ref 10), specially designed for rotor-triggered measurements. Key specifications of the TEDAS III DAQ system are:

- 496 channels analogue DAQ
- Simultaneous sampling
- 1024/2048 samples per revolution
- 16-bit ADCs
- ±5 V buffered signal input
- Up to 3000 rpm = 50 Hz sampling
- 100 MB/s data volume for internal ring buffer
- Rotor triggered measurement or fixed frequency
- Independent simulator/rotor switching

A so called “AmpBox”, specially designed for the usage within wind tunnel models, is used for strain gauge sensor supply and signal conditioning of up to 48 input channels. The output of the amplified signals is in the range of 0 to +5V and directly connected to the TEDAS signal input. The millivolt signal from a strain gauge is connected to programmable gain amplifiers (PGA) which allow offset adjustment to reach the correct output range. The parameters can be remotely adjusted by a sophisticated network-communication interface via Ethernet. No hardware changes or soldering is necessary. Apart from the PGAs, the AmpBox contains constant-current sources for PT100 temperature sensor supply.

5.3. Data acquisition rotating sensors

Because of the limited space only very small signal conditioning and slip ring systems mechanically fits within the model. Thus, it’s a challenge to measure the required number of sensors in the rotating frame. That’s why all data from sensors in the rotating frame are measured using a newly developed wireless rotational DAQ system (Ref 11). A small slip ring with a limited number of channels is used for transfer of electrical power to the rotating parts. The rotational DAQ is placed on top of the main rotor head (see Figure 15) in an ellipsoid shaped housing carrying the electronic components. The lower housing part is made from aluminum and screwed to the rotor head.

The PCBs are mounted on this supporting structure. The top lid which closes the housing is made from a 3D-printed plastic material allowing radio frequencies to pass through. The wireless DAQ system is divided into analog signal conditioning, an Analog to Digital

Conversion frontend (real time, fixed clock), and an embedded systems part. The Linux-based embedded system is required for gathering all of the data from the six ADC frontends via an SPI bus, time stamping the data packets and providing a TCP server connection for the Wi-Fi transmission path.

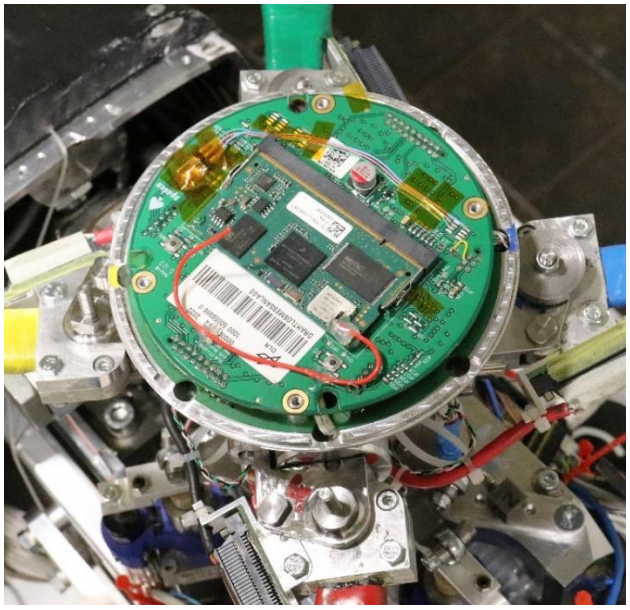

Figure 15: Rotational DAQ system

In total 48 channels can be measured with a fixed data rate of up to $50\ kSamples/s$. Due to the system architecture no continuous measurement of many revolutions is possible. Instead a predefined number of samples are transferred per message s Via the small slipring the 1P signal from the non-rotating frame is transferred to the rotating frames as well to get the possibility for data synchronization and resampling to rotor revolutions in the aftermath to analyze and synchronize the streams of both DAQ systems.

5.4. External data server

Beside the fast sampling TEDAS DAQ there are software tools available for an exchange of static data (e.g. wind tunnel speed, humidity, temperatures) between different local or external parties. BUDDI (Basic Utility for Double Data Interchange) is a network-based TCP server application that responds to incoming client requests running in the local network. The update rate for reading and writing data is about $1\ Hz$. Multiple client requests can be handled via multiple threads. The server manages the data with a time stamp for every writing action and stores the data on hard disk beside buffering a defined amount of data in the RAM. Clients can request data for a defined time stamp or read latest data.

6. PRETESTS

Prior to the final wind tunnel test a lot of pre-test activities are necessary. As described in section 4.1 the slat pack was loaded in a long-time test to guarantee the fatigue strength of the last design. Before final blade manufacturing the root part of a preliminary rotor blade was tested in a hydraulic test bench, as can be seen in Figure 16, to simulate centrifugal loads and blade bending moments in flap and lead-lag direction. For data monitoring also strain gauges were installed. The long-time test included two different load conditions simulating nominal rpm and 115% of nominal rpm (up to $7.2\ kN$) with their corresponding blade bending moments of up to $40\ Nm$ each for flap and lead-lag. Each condition was tested for 100000 cycles. Since no damage could be observed, the manufacturing concept was proven to be ok and after that the manufacturing of the five rotor blades was started.

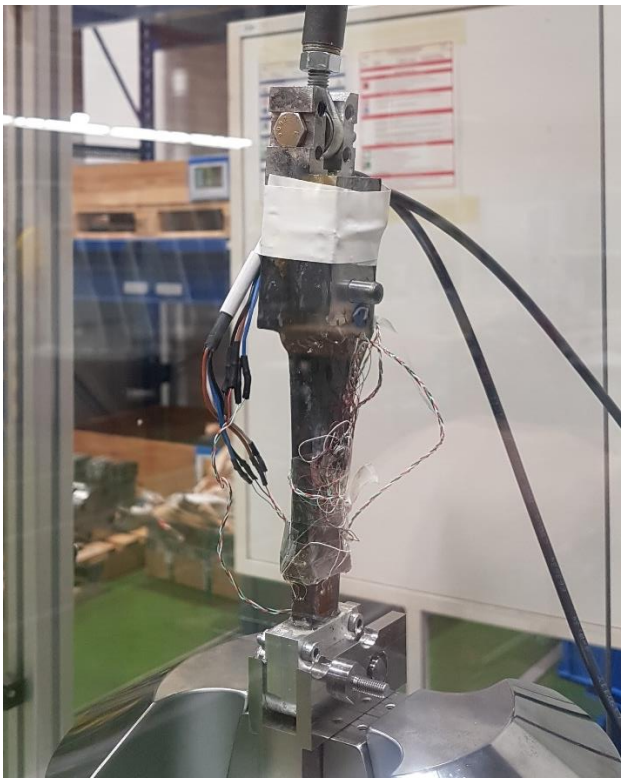

Figure 16: Blade root section in hydraulic test bench

6.1. Whirl tower test

To guarantee the functionality of the rotor blades each one was tested individually in the DLR whirl tower facility. A special rotor head was designed to mount a rotor blade on one side and a counter weight on the other side, as shown in Figure 17. No pre-cone angle is used. Manual pitch angle changes are possible by a screw drive. The main drive of the test rig, which is based on a $47\ kW$ electric motor and a belt drive system, had to be modified to reach a maximum rotor speed of $3000\ rpm$. Therefore, the pinion and the belt were exchanged. The test rig setup is shown in Figure 18.

A rough in-situ calibration of each rotor blade was done to get information of blade loads and dynamics during rotation. Measurements of blade flap bending, lead-lag bending and torsion moment could be done without additional head electronics but using a direct connection of the strain gauge bridges with the amplifier via a small slip-ring system below the rotor system. After the rotor balancing procedure each rotor blade was driven up to $2500\ rpm$, which means about 120% of nominal centrifugal load since the rotor radius is increased by about $100\ mm$ at this test rig. No re-balancing was necessary for the other blades. For each blade two spin-up tests were conducted up to $2500\ rpm$ with two different angles of incidence $(+3\ deg, +8\ deg)$.

A very similar behavior was found comparing the flap bending (Figure 19), lead-lag bending and torsion moments versus rotor speed. Finally, all four rotor blades passed the whirl tower test successfully and were ready for use in the complete rotor configuration.

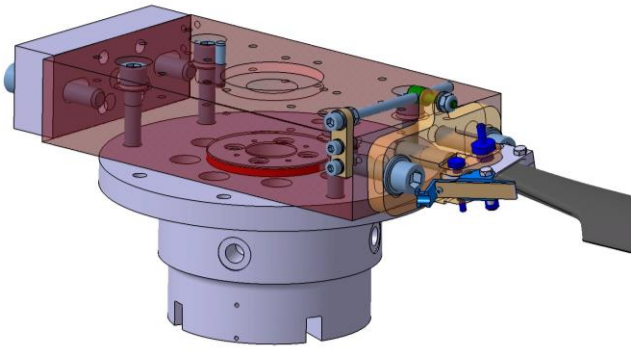

Figure 17: Rotor head for whirl tower tests

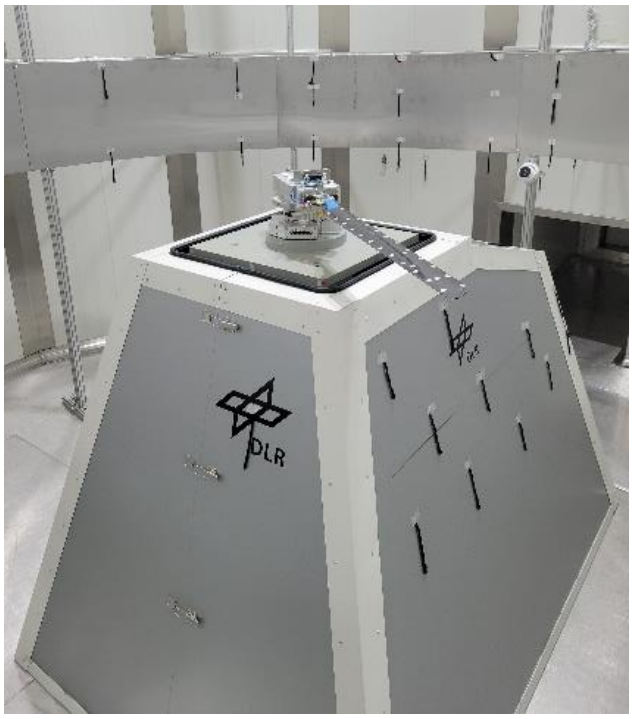

Figure 18: Single rotor blade at whirl tower

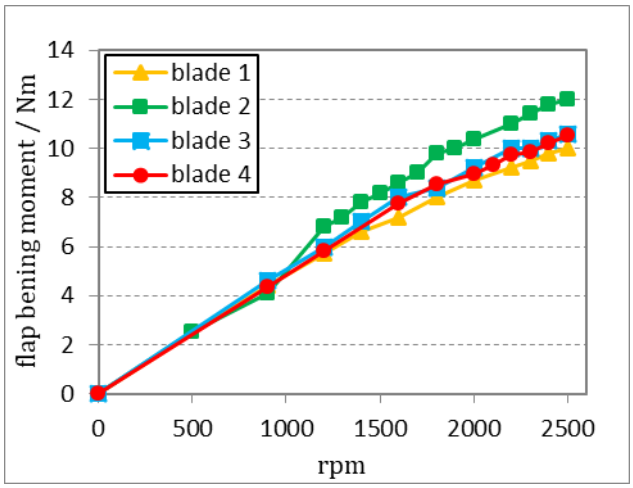

Figure 19: Flap bending moment vs. rotor speed

6.2. Pre-testing of complete system

Prior to the wind tunnel tests the complete system is checked in the DLR-FT rotor hall. The model was mounted on a metal frame and all connections were installed as they are in the wind tunnel test. After calibration of all model sensors (see section 5.1) and a ground vibration test the new rotor system was started for the first time, initially without fuselage as can be seen in Figure 20. Using the blade tip lights, the adjustment of correct blade tracking was an easy task. Fine-tuning was done by changing the pitch link length. Thereafter rotor balancing was the next step.

This is usually done based on information of the rotor balance. A very linear behavior was found and a fine balancing was conducted for the rotor with blade stubs as well as for the complete rotor system with blades.

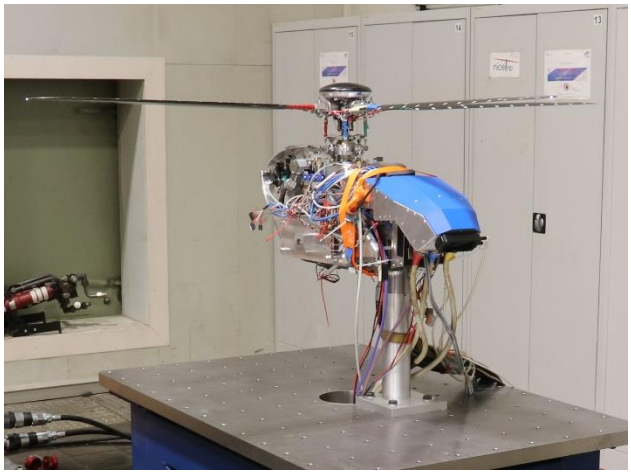

Figure 20: Model pre-test without fuselage

Furthermore, the fuselage shells were mounted and pre-tests in full configuration took place (Figure 21) to check the functionality of each subsystem. The pre-test included several rotor starts up to nominal rpm, hydraulic parameter optimizations, thrust variations as well as variations of cyclic pitch inputs. The newly developed rotating DAQ system was successfully put into operation during this pre-test phase.

Figure 21: Model pre-test at DLR-FT rotor hall

7. WIND TUNNEL TESTS

Up to now two wind tunnel tests were conducted using the new model. During the first wind tunnel test in 2020 the two different fuselage configurations REF (see Figure 22 + Figure 23) and SZ-1 (Figure 24) were tested as “fuselage only” arrangements with and without a rotor hub dummy with blade stubs included in a seven days campaign. The dummy rotor hub was able to spin-up to the nominal rotor speed. The test matrix included changes of wind speed between $20\,m/s$ and $80\,m/s$ in different steps, while at each wind speed variations of model angle of attack (α) and model yaw angle (β) were performed. In total 150 polars were measured with 1700 data points.

As an example, a comparison of the drag force coefficient versus angle of attack is shown in Figure 25 for the different configurations. A reduction of total drag is clearly visible for the SZ-1 configuration almost over the complete α-range both for non-rotating hub (REF-N vs. SZ1-N) and rotating hub (REF-R vs. SZ1-R). The skids at the REF-configuration leads to about $40\,\%$ drag increase rotating hub (REF-NK vs. REF-N). The influence of the spinning rotor dummy is different for both fuselages. While for the SZ-1 fuselage a difference is only visible at higher α, the differences for the REF-fuselage are present over the complete α-range.

Figure 22: REF fuselage with dummy rotor system at DNW-NWB

Testing in “isolated fuselage only” configuration was finished in the wind tunnel campaign in 2020. Thus, a huge data base is available for code validations and further analysis.

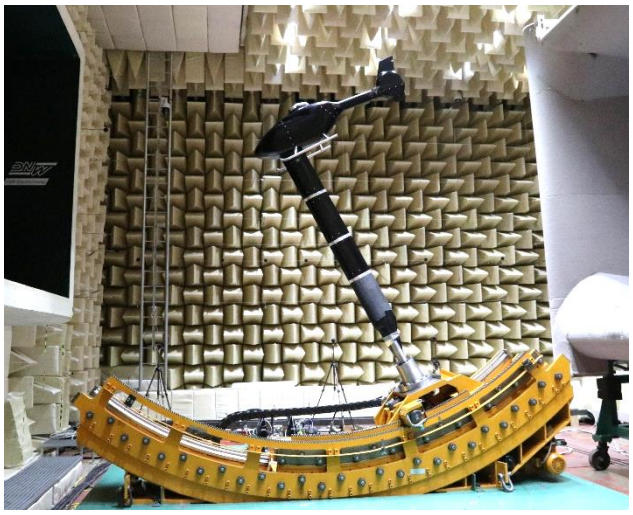

Figure 23: REF fuselage with skids without rotor

Figure 24: SZ-1 fuselage with dummy rotor system at DNW-NWB

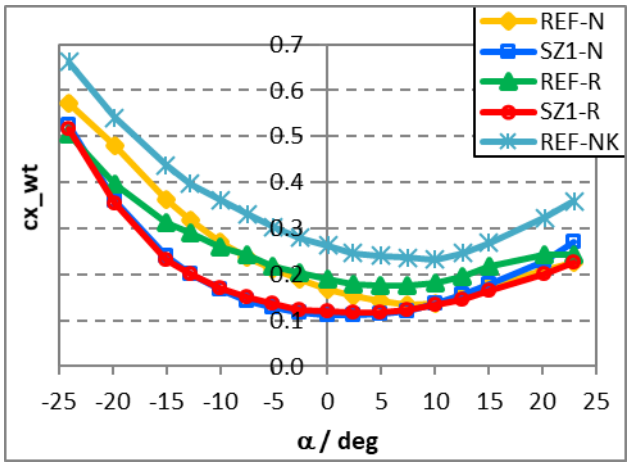

Figure 25: Drag force coefficient vs. angle of attack (N=non-rotating, R=rotating, K=skids)

In 2023 the rotor blade manufacturing was finished and each blade has successfully passed the individual blade spinning test at DLR's whirl tower facility.

In June 2024 a second wind tunnel test was conducted at DNW-NWB with the fully equipped model including spinning rotor with fully remote-controlled swash plate system and additional wings. For this test the rotor speed was limited to 75% of nominal rotor speed due to required safety factors, which corresponds to $1860\,rpm$ or $195\,rad/s$. In a three-week test campaign, repeat measurements of the isolated SZ-1 fuselage were performed first to compare with the results from 2020. Main objectives of this test were rotor performance, aerodynamic interactions between rotor and fuselage including the additional wings, acoustic measurements and investigations to slowed rotor conditions. In Figure 26 the test setup is shown.

To get acoustic data from below the model two microphone arrays were installed, one on the advancing side on the upstream location of and on the retreating side of the rotor on the downstream location. The arrays are mounted on the so called "alpha-beta support" and are moving together with the side slip angle movement in β-direction. When model angle of attack α is changed, the relative position between rotor and microphone arrays is changed as well. Each array carries 28 microphones, so in total acoustic data from 56 microphone positions are available for further noise analyses.

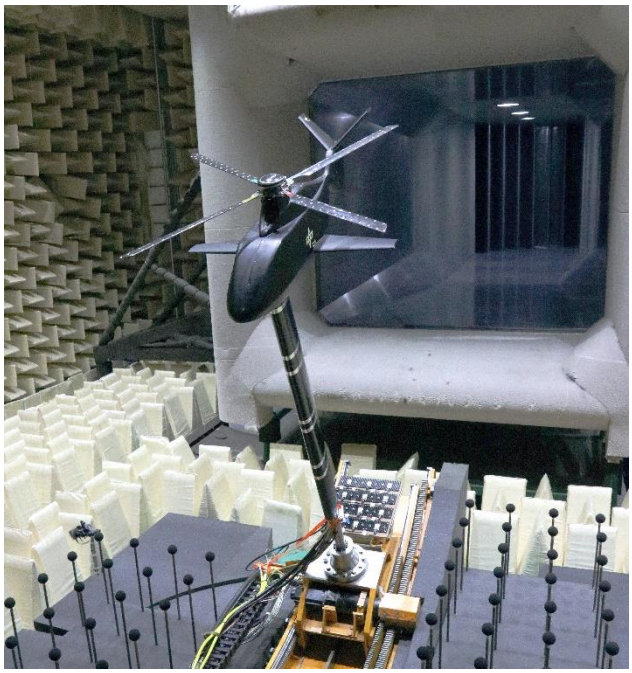

Figure 26: SZ-1 test at DNW-NWB

Trimming of the model was done with respect to a scaled virtual weight in combination with zero rolling and pitching moments at the fuselage reference point

by adjusting collective and cyclic blade pitch angles. To trim the propulsive force also model angle of attack α was used and adjusted by NWB. Thus, a close cooperation between model pilot and wind tunnel operator was necessary.

7.1. Rotor Figure of Merit (FM)

The rotor efficiency was experimentally evaluated by means of a sweep in the collective control angle Θ_{75}, which was calibrated to the 75 % radial position of the non-rotating rotor blade. Results are based on a thrust sweep at the open NWB test section while the rotor angle was at zero α. The open jet configuration of the test section allows the rotor downwash to freely move downwards towards the ground at a distance of ca. 4 R below the rotor, therefore free of ground effect. Because of the closed test hall some unknown recirculation will have been in effect, but it could not be measured.

Another issue affecting the data is based on the construction of the hydraulic drive system, whose hydraulic hoses bypass the rotor balance. Once hydraulic pressure is put on the hoses the rotor balance measured an offset mainly in the x- and z-direction, but not in the moment about the z-axis. The latter was used to compute the rotor power. Therefore, the balance offset developing in F_z with very slowly rotating rotor was also measured and subtracted from the values at nominal speed or rotation. The dependency of the offsets with respect to rotor power changes could not be evaluated and remains unknown.

Prior to all measurements with rotor blades, a sequence of measurements with blade stubs was executed both in non-rotating and in rotation with nominal speed. These ranged from hover to the highest wind speed as well as all ranges of model incidence angles. The purpose was to identify the hub tare loads in F_x, F_z and rotor power P due to the aerodynamic hub fairing and the drag of the blade roots. These tare loads were then already subtracted from all data measured with the rotor blades.

Finally, the rotor balance revealed a drift in its offsets versus time of measurement. To allow correction of this offset drift reference measurements were taken before and after each sequence of hover measurements. The difference in offset can then be subtracted from the data between begin and end of the measurements, assuming a linear variation from begin to the end of a sequence.

The result for the thrust in hover condition and power measurements versus the collective control angle after the above corrections were introduced is shown in Figure 27. Three configurations are included in the figure: circle symbols represent the rotor without fuselage fairing and without wings attached, solid dots the rotor plus fuselage attached, and the open square is the configuration with additional wings on both sides underneath the rotor and within the rotor downwash. In addition, the ideal power is indicated, which was computed from the thrust using simple momentum theory.

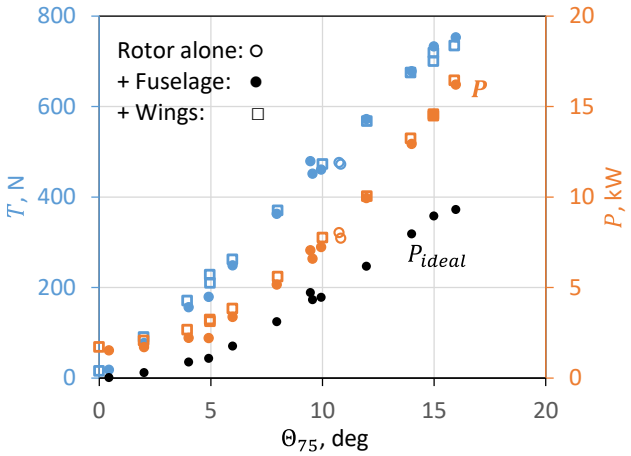

Figure 27: Thrust and power measurements in hover for different configurations

The thrust is about zero for zero collective control angle, then rises with increasing Θ_{75} as expected, until from $\Theta_{75} \approx 15°$ on some sort of stall onset can be observed. The power curve is non-zero at zero thrust because of the remaining airfoil drag acting on the blades, then rises exponentially with increasing thrust and continues to rise where stall onset is observed at the largest control angles.

The inclusion of wings underneath the rotor was expected to show some thrust increase due to the blockage of the rotor downwash, similar to a ground effect. Up to $\Theta_{75} \approx 10°$ this actually can be observed in the data, but at high thrust conditions the thrust is little less than without wings. The rotor power appears slightly larger than for the configuration without wings throughout the range of thrust, even at zero thrust, where the winds cannot have an impact on the rotor

any more. Therefore, the offset at zero thrust is further used to correct the data with wings mounted.

The third configuration is the rotor alone, i.e., no wings and no fuselage fairing underneath the rotor. Only a few data were taken near $\Theta_{75} = 11°$, denoted by open circles in Figure 27. The missing fuselage and with it the smaller blockage of the rotor downwash results in little less thrust at a given collective control angle.

Small variations in rotor speed of rotation and air density were measured during that run, therefore the non-dimensional data of specific power coefficient C_P/σ versus the specific blade loading coefficient C_T/σ is shown next in Figure 28, also the above correction for power at zero thrust is applied. The power curve of rotor + fuselage and + wings coincide now, only at the highest thrust values the inclusion of wings appears to require even more power than without. It must be noted that the fuselage and wing downloads were not yet considered here; the sum of rotor thrust, fuselage and wings downloads will significantly reduce the total vertical force. To perform the hovering case, the rotor thrust also would have to overcome all these downloads.

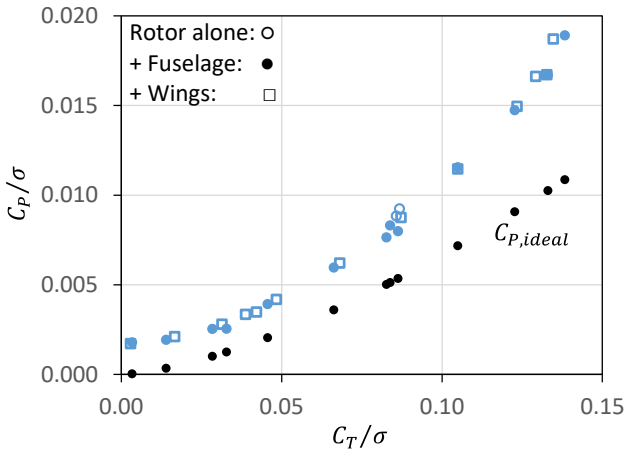

Figure 28: Power coefficient versus specific blade loading coefficient

Finally, the resulting rotor figure of merit (FM), defined as the ratio of ideal power to real power, can be computed, which combines thrust and power required to generate the thrust in one graph. The figure of merit is given in Figure 29 and based on the data shown before. The scatter indicates the variations to be expected when repeating measurements. The first measurement of this run was at $C_T/\sigma = 0.033$ and the second measurement at $C_T/\sigma = 0.083$, both are above the FM curve. It can be assumed that these two were taken before the recirculation according to the thrust was fully developed, but this is a hypothesis.

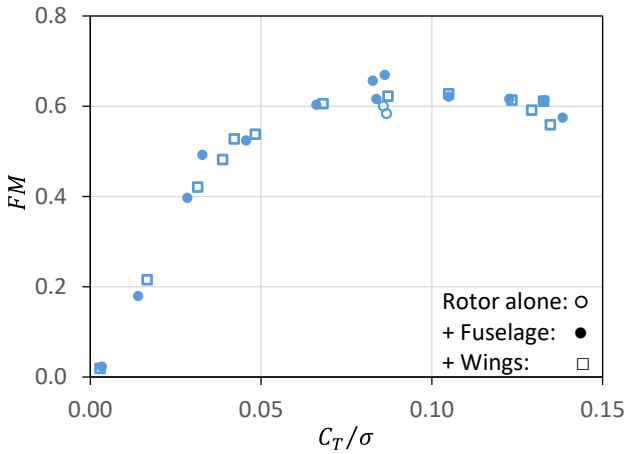

Figure 29: Figure of merit curve for the rotor

The configuration with fuselage and wings results in the same FM curve, except for the highest thrust conditions, where without the wings slightly better rotor efficiency is observed. In either configuration rotor stall onset is obviously reached, indicated by a reduction of FM. The omission of both wings and fuselage (indicated by circle symbols) near $C_T/\sigma = 0.087$ supports the assumption that the reduction of blockage of the rotor downwash in this configuration increases the power because of slightly increased downwash.

Overall, the data, after proper correction of the known offsets, indicate a good repeatability and consistency. Further analysis will also address the blade bending in flap, lag and torsion. These data are a good basis for code validation, extending the hovering polar up to the stall onset regime, which is rarely reached in hovering rotor measurements.

8. CONCLUSIONS

A new medium size wind tunnel model was developed in the framework of the DLR guiding concept “The Rescue Helicopter 2030” in two different DLR projects

1. According to the requirements a suited load balance concept was conceived and the functionality could be proven in pre-tests and wind tunnel tests.

2. Most of the model construction and manufacturing of model components like basic structure or rotor blades was done in-house at DLR.
3. Model instrumentation has been selected according to the different purposes and specifications, implemented and finally calibrated to be ready for use.
4. For the new model two different DAQ systems are used, the longstanding TEDAS III for the non-rotating data and a special designed new rotating DAQ, located in the rotor hub.
5. Preliminary results from pre-testing and from two wind tunnel tests show that the new model is ready for usage in upcoming wind tunnel campaigns.

Author contact:

Oliver Schneider, oliver.schneider@dlr.de

Henning Mainz, henning.mainz@dlr.de

Erik Brehl, erik.brehl@dlr.de

Sascha Henseleit-Wieser sascha.henseleit@dlr.de

Berend G. van der Wall berend.vanderwall@dlr.de

9. REFERENCES

1. van der Wall, Berend G. and Burley, C.L. and Yu, Y. and Richard, H. and Pengel, K. and Beaumier, P. (2004) “The HART II Test - Measurement of Helicopter Rotor Wakes.”, *Aerospace Science and Technology*, 8 (4), pp 273-284.
2. van der Wall, Berend G. and Lim, Joon W. and Smith, Marilyn J. and Jung, Sung N. and Bailly, Joelle and Baeder, James D. and Boyd, Douglas D. Jr. (2013) “The HART II International Workshop: An Assessment of the State-of-the-Art in Comprehensive Code Prediction.” *CEAS Aeronautical Journal*, 4 (3), pp 223-252. Springer. doi: 10.1007/s13272-013-0077-9, ISSN 1869-5582.
3. Raffel, M. and de Gregorio, F. and de Groot, K. and Schneider, O. and Gibertini, G. and Seraudie, A. “On the Generation of a Helicopter Aerodynamic Database”, *The Aeronautical Journal*, 2010, 115 (1164), pp 103-112. Cambridge University Press. ISSN 0001-9240
4. Küfmann, P. and Bartels, R. and van der Wall, Berend G. and Schneider, O. and Holthusen, H. and Gomes, J., “The First Wind Tunnel Test of the Multiple Swashplate System: Test Procedure and Principal Results”, *Journal of the American Helicopter Society*, 2017, pp 1-13, DOI: 10.4050/JAHS.62.042002, ISSN 0002-8711
5. Geurts, E. and Schneider, O. and Bernini, G. and Battiston, A. and Ponza, R., “NEXTTRIP Interactional aerodynamic assessment of an advanced tilt rotor configuration” 47th European Rotorcraft Forum, Glasgow, Scotland, 7-10 September, 2021
6. van't Hoff, S. and Fonte, F. and Schneider, O. and Soul, K. and Kapteijn, K., “Whirl Flutter Testing of ATTILA Tiltrotor Testbed” The Vertical Flight Society's 80th Annual Forum, May 2024, Montreal, Canada
7. Schwermer, T. and Gardner, A. and Raffel, M. “Dynamic Stall Experiments on a Rotor with High Cyclic Setting in Axial Inflow” American Helicopter Society (AHS): 73rd Annual Forum & Technology Display, 09.-11. Mai 2017, Fort Worth, Texas, USA.
8. Schneider, O., “Analysis of SPR measurements from HART II”, *Aerospace Science and Technology*, 9 (5), pages 409-420, Elsevier, 2005
9. Mainz, H., “Design, Manufacturing And Testing Of Highly Instrumented Rotor Blades For A Medium Size Helicopter Wind Tunnel Model”, 50th European Rotorcraft Forum, Marseille, France, 10-12 September, 2024
10. Gelhaar, B. (2000) “TEDAS II - High Speed Data Acquisition, Storage and Distribution.”, European Telemetry Conference, pp 97-108., Garmisch-Partenkirchen, 22-25 May 2000
11. Brehl, E. and Schneider, O. “Rotational Data Acquisition for Rotorcraft Wind Tunnel Models”, European Test and Telemetry Conference, Paper 3596, Toulouse, France, 13-14 June 2023

10. CLASSIFICATION & COPYRIGHT

The paper must be unclassified for release to the public and cleared by the appropriate company and/or government agency if necessary. CEAS and its national member societies shall be allowed to publish the paper. The copyright information is stated on the Forum website https://www.rotorcraft-forum.eu/ and on the front page of this template. All papers presented at the ERF will be published as ERF proceedings. In addition they will be available in a freely accessible web-based repository 2 years after the respective conference.